**Discover** Mechanical Engineering

Research

# Flow characteristics of sintered titanium-based porous transport layers using machine learning

**Dieter Froning[1] · Eugen Hoppe[1] · Martin Müller[1] · Ralf Peters[1,2]**

Received: 2 August 2024 / Accepted: 10 January 2025
Published online: 20 January 2025
© The Author(s) 2025 OPEN

**Abstract**
Porous transport layers, sintered from sphere-based titanium material, can be used in electrolyzers. A sedimentation-based stochastic sphere model was used to create many versions of a sphere-based micro-structure. Aided by Lattice-Boltzmann simulations, the permeability was calculated based on the artificial micro-structures. These data were then used to train a convolutional neural network in order to characterize material on the basis of its micro-structure. Binary image series from the real material of porous transport layers were characterized using a deep learning model trained with artificial data. A reasonable degree of accuracy was achieved by the neural network in the prediction of the through-plane permeability of the real material, when the samples were manufactured from spherical particles.

**Graphic Abstract**

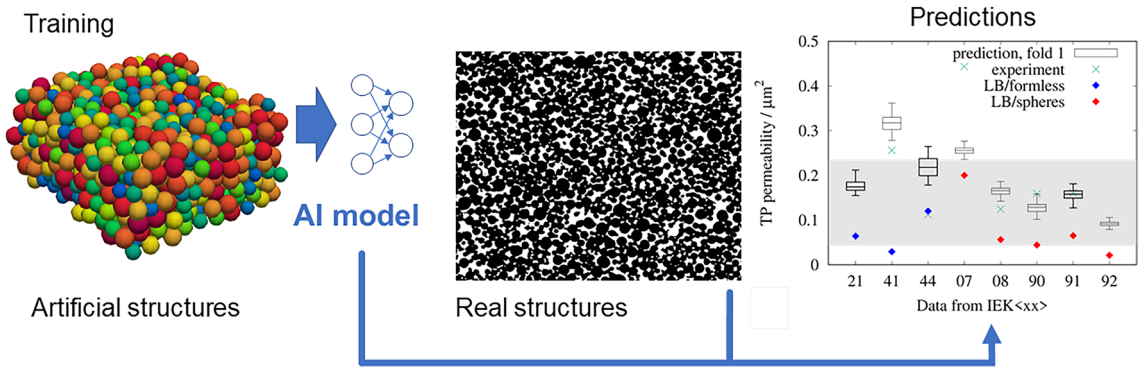


**Keywords** Electrolysis · Porous transport layer · Lattice-Boltzmann · Stochastic modeling · Deep learning

✉ Dieter Froning, d.froning@fz-juelich.de; Eugen Hoppe, e.hoppe@fz-juelich.de; Martin Müller, mar.mueller@fz-juelich.de; Ralf Peters, ra.peters@fz-juelich.de | [1]Institute of Energy Technologies, IET-4: Electrochemical Process Engineering, Forschungszentrum Jülich GmbH, Wilhelm-Johnen-Straße, Jülich 52425, NRW, Germany. [2]Fakultät für Maschinenbau, Ruhr-Universität Bochum, Universitätsstraße 150, Bochum 44801, NRW, Germany.

## 1 Introduction

The optimization of electrolyzers is crucial for the better utilization of resources in the ongoing energy transition. One component of electrolyzer stacks is the porous transport layer (PTL), the geometric structures of which at the µm level can affect transport properties. The permeability, for instance, is relevant to fluid transport at the macroscopic level. Given a particular material, the permeability can be obtained experimentally [1–3] or by transport simulations using Darcy's law [4–7]—except under complex or extreme conditions [8]. The Lattice Boltzmann (LB) method is applied by various researchers to geometric structures in the micrometer range. Tomadakis et al. [4] investigated generic artificial fiber arrangements. Nabovati et al. [5] as well as Froning et al. [6] used different kinds of fibrous micro-structures of gas diffusion layers (GDLs). Regarding the transition from the lab scale to larger ones, different kinds of PTLs were investigated by Janßen et al. [9] Transport simulation across scales was also investigated by Beale et al. [10], who resolved the micro-structure of the porous layer in the channel/PTL assembly of a fuel cell.

Yuan et al. [11] conducted a review of different kinds of PTLs and their properties. Several PTLs for a proton exchange membrane (PEM) electrolzer were investigated by Panchenko et al. [12] using neutron spectroscopy. A segmented PEM electrolyzer was used by Parra-Restrepo et al. [13] to analyze the influence of PTL properties on mass and charge transfer. Meanwhile, Park et al. [14] compared the performance of PEM water electrolysis (PEMWE) from the viewpoint of flow field geometry with and without PTLs by means of two-phase flow simulations. Furthermore, using flow simulations, Lopata et al. [15] optimized the electrochemical reactions by adjusting the permeabilities of the PTLs. Schuler et al. [16] analyzed the micro-structure of fiber-based PTLs using X-ray tomographic microscopy. The hetereogeneous structure of microporous layers in fuel cells was analyzed by Chen at el. [17], also utilizing X-ray tomography. Titanium-based PTL structures were experimentally analyzed by Höh [18], as well as by Borah [19]. The micro-structure of titanium-based PTLs was optimized by Xu et al. [20], who calculated the permeability of their artificial material using Lattice-Boltzmann (LB) simulations. Bhaskaran et al. [21] also implemented LB simulations to study PTLs for water electrolysis. In turn, Liu et al. [22] investigated the relationship between topology and the transport properties of fiber-based PTLs. For fiber-based porous materials, machine learning (ML) approaches were applied by Cawte and Bazylak [23], as well as Froning et al. [24] Kamrava et al. [25] trained a deep learning (DL) network with artificial data in order to predict the permeability of real porous material. A different training method was applied by Qian et al. [26] for their convolutional neural network (CNN) in order to predict the permeability of porous material, which was then applied to complex structures. The benefit of artificial data is its availability in numerous samples. This is necessary for supervised learning. Real data, however, can embed hidden morphologic features affecting the reliability of CNNs that were trained without these features. Such drawback was found by Froning et al. [24] in case of fibrous micro-structures of GDLs.

LB simulations are one of the state-of-the-art methods in the determination of the permeability of porous material, once the three-dimensional (3D) micro-structure is given. A disadvantage is the requirement of high performance computers (HPC). Also operating with geometrical structures, ML methods can fast predict features from a given micro-structure, once a model was trained properly. The training requires many data being stochastic equivalent to the targeted application's micro-structures. The use of artificial micro-structures that are stochastic equivalent to real data have been used successfully in LB simulations of GDLs using LB simulations [6, 27]. In previous work, artificial data were used for the training of a CNN in order to predict the permeability of fiber-based micro-structures [6, 24]. The challenge is the proper specification of artificial data that covers the real material in the sense of hidden features identified by CNNs. In this study, a CNN was developed and trained with artificial data to predict the permeability of real material based on sintered titanium particles. Havemann [28] developed a stochastic sphere-based sedimentation model for the representation of the micro-structure of titanium-based PTLs. The micro-structures of the material investigated by Borah [19] were provided by Froning and Müller [29]. In the next section the data of the sintered material of Borah [19] were presented, as well as the sedimentation model of Havemann [28], which can generate realizations of artificial micro-structures. The methods, introduced in Sect. 3, involve LB simulation, Havemann's sphere model [28], the CNN, its data preparation and short remarks on the training. The validation of the resulting DL model is presented in Sect. 4. Afterwards the results of the application of the CNN to the real data of Borah [19, 29] are presented. Finally the results are discussed and some conclusions drawn.

The data flow discussed in the manuscript is illustrated in Fig. 1. There are two sources of 3D micro-structures involved, artificial and real data. Through-plane (TP) permeabilities were provided by experiments of Borah [19]. The permeabilities of artificial data were calculated using LB simulations. Furthermore, a CNN trained with artificial data, was used to predict the permeability of real 3D micro-structures.

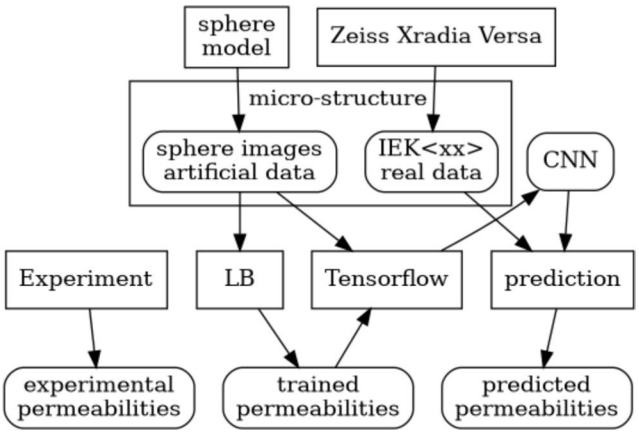


**Fig. 1** Overview of the data flow

## 2 Data

The data provided by Froning and Müller [29] was experimentally analyzed by Borah [19], according to whom the materials IEK07, IEK08, IEK90, IEK91, and IEK92 were created by sintering titanium powder consisting of spheres with diameters of 45 µm. Höh observed a shrinkage of 3–10% during the sintering process of such materials [18].

### 2.1 Real data

The micro-structures of eight samples of titanium-based PTLs are available as segmented binary image series devised by Froning and Müller [29]. The underlying material was experimentally analyzed by Borah [19] who measured the through-plane (TP) and in-plane (IP) permeability and compared the experimental results with simulations using different simulation methods. Comparing the simulation results from pore network modeling (OpenPNM), voxel-based computation (GeoDict), volume-of-fluid-based computational fluid dynamics (CFD, ANSYS/Fluent) and the LB method (Palabos), Borah identified GeoDict and Palabos as the most precise numerical methods for obtaining the permeability of the material.

The binary image series [29] are labelled IEK07, IEK08, IEK21, IEK41, IEK44, IEK90, IEK90, IEK91, and IEK92. Figure 2 shows one typical image of each series with a resolution of 1 µm/px. The z-coordinate is along the image number of the series.

The samples of the material were sintered from two different kinds of particles. IEK07, IEK08, IEK90, IEK91, and IEK92 were spherical particles with a diameter of 45 µm, with the other samples (IEK21, IEK41, and IEK44) being

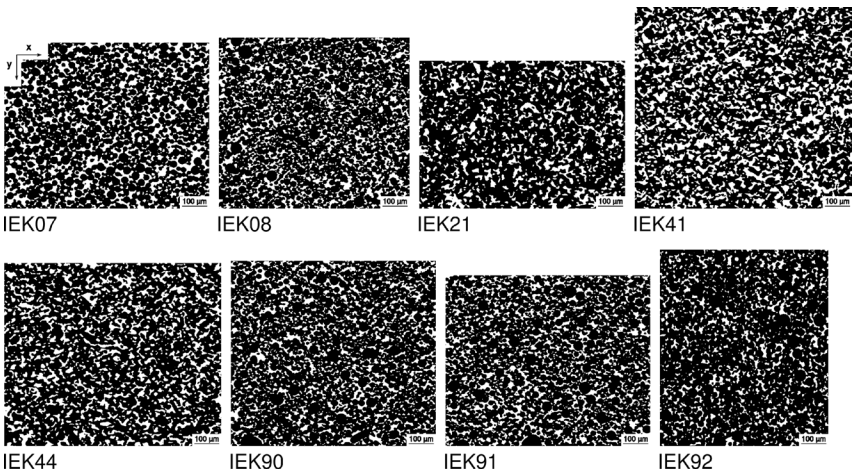


**Fig. 2** Images with a resolution of 1 µm/px of a Pt-based PTL material; labels according to Froning and Müller [29]

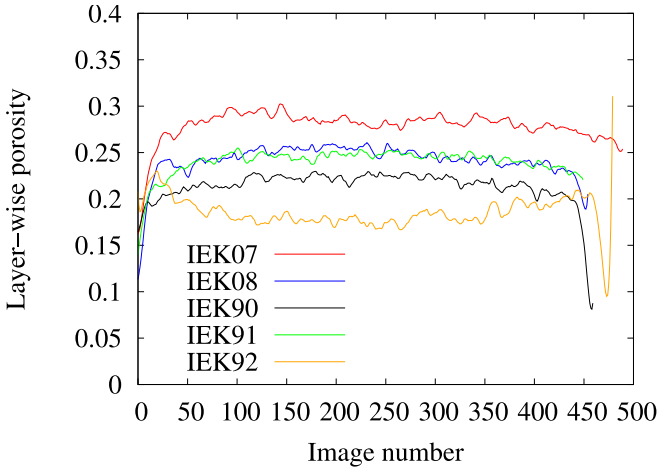


**Fig. 3** Layer-wise porosity of the image series of the sphere-based material

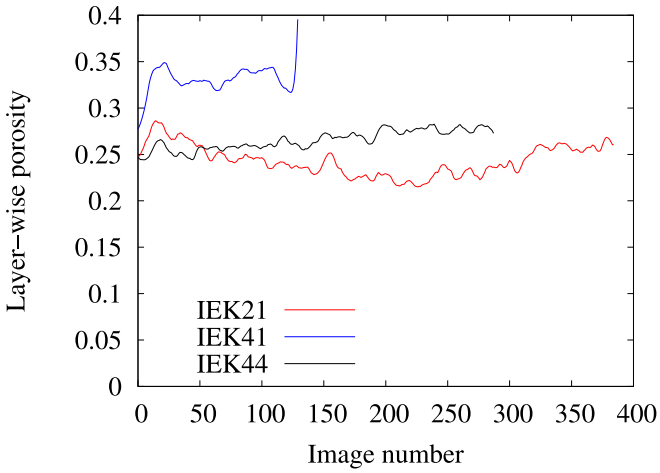


**Fig. 4** Layer-wise porosity of the image series of the material based on formless particles

created from formless particles. The materials were manufactured by two vendors. The spherical particles represent gas-atomized spherical titanium powers with diameters less than 45 µm [30]. The formless particles were fabricated using a hydride-dedydride (HDH) process, resulting in shapeless particles [31]. In both cases the sintering process lets particles conglomerate, resulting in morphologies that look similar to human eyes.

The images on the top and bottom of the series are influenced by the surface of the samples. The impact of the outer surface is shown in Figs. 3 and 4 where the two-dimensional (2D) layer-wise porosity is displayed along the image stack. The layer-wise porosity is the amount of white space in Fig. 2. Without any influence the profiles should show statistical variations according to the irregular micro-structure. This is in fact the case for the major region, which is not too close to the surface of the material.

For the processing of the data, 50 images were omitted from the top and bottom of each of the image stacks that can be downloaded from the Jülich DATA repository [29]. For IEK41, this was not possible, as this sample only contains 130 images. The reason for this procedure includes artifacts caused by the surface of the samples. The same method was applied for the LB simulations presented by Borah [19].

## 2.2 Artificial data

Motivated by the spherical origin of the majority of the samples from Sect. 2.1, a geometric model was developed by Havemann to create irregular structures based on spheres [28].

Drawing on a sedimentation model by Elsner [32], a geometric model was developed to create an irregular structure from spheres with different diameters. To mimic the deformation of the spheres by the sintering process of the real material, the artificial spheres were allowed to overlap each other. Figure 5 shows an example. Because of disturbances on the

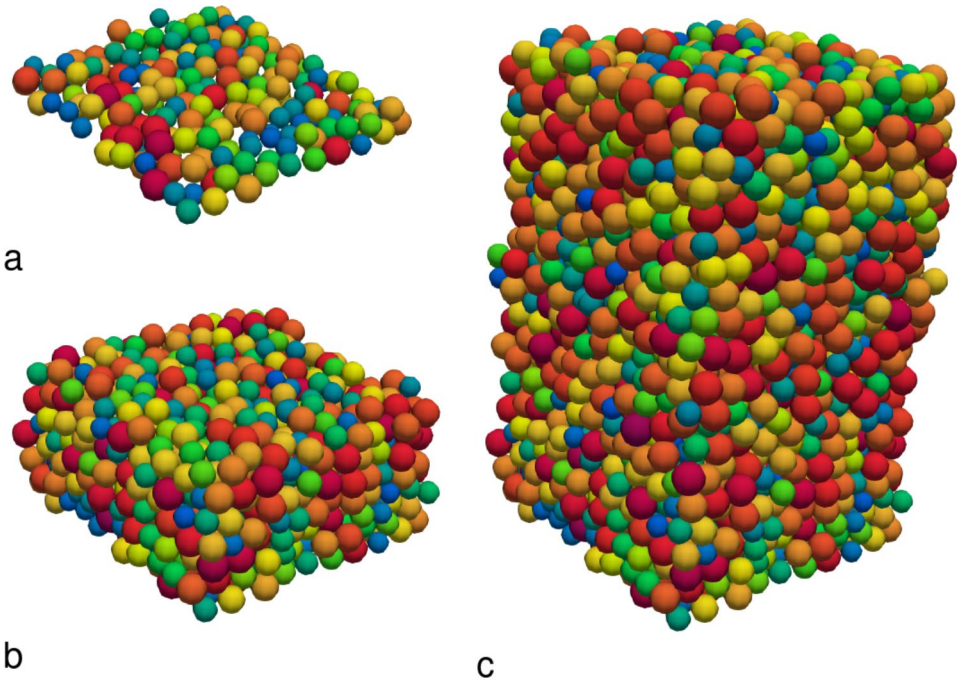


**Fig. 5** Set of spheres in different stages of development, colored according to their diameter: blue is small, red is large; **a** initialization layer and beginning of sedimentation; **b** sedimentation up to one-third of the desired height; **c** extraction of a 200 µm x 200 µm x 200 µm subsection from a completely filled domain

bottom and top of the sphere packing [28], the desired section was cut out of a domain that is larger in the z-direction, as depicted in Fig. 5.

The calculated sphere packing is represented as a list of spheres, each of them specified by their positions and radii. Additionally, a series of black/white (BW) images was created, suitable for specifying the micro-structure for LB simulations based on an equidistant grid [33].

## 3 Methods

The TP permeability of the 3D morphology of the porous material was obtained from transport simulations as shown in Sect. 3.1. The structure of the real material [19, 29] was obtained from a Zeiss Xradia 410 Versa µ-CT machine.

### 3.1 Lattice-Boltzmann simulations

The single phase transport of a fluid through a porous micro-structure was simulated using the LB method. From the resulting 3D velocity and pressure fields, the permeability $\kappa$ of the irregular porous structure was calculated using Darcy's law

$$\kappa = -\frac{q \cdot \mu}{\nabla P} \tag{1}$$

the pressure drop $\nabla P$, the flux $q$ and the dynamic viscosity $\mu$. This method was applied earlier to different materials [24]. Considering that the images are in the plane of a planar material, the transport direction of the fluid flow is the z-coordinate, being the TP direction of the material.

A benefit of the LB method for simulating gas transport in porous material is the potential of geometry specification by a series of BW images [4, 5, 27]. In Fig. 6, four images are exemplarily shown along the z direction. Especially for irregular micro-structures this is an advantage over the requirement of mesh generation in case of volume-of-fluid methods.

The results of the LB simulations on real PTL material have been experimentally validated by Borah [19], as mentioned in Sect. 2.1. The results of LB simulations on different kinds of artificial data were validated by Froning et al. [6, 27]. Results of LB simulations on the sphere model were investigated by Bukka [34].

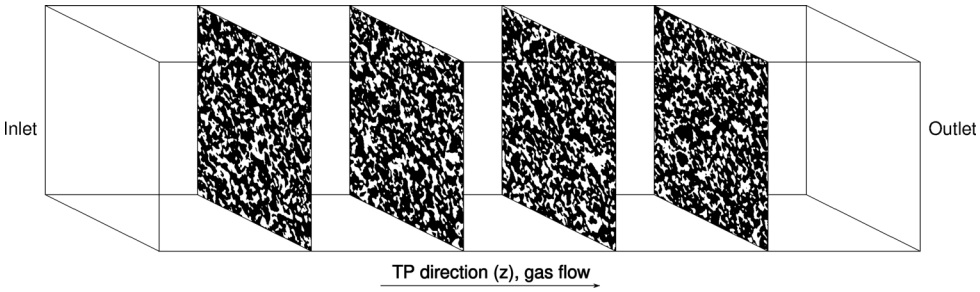


**Fig. 6** BW images for geometry specification of the LB method

### 3.2 Spherical model

The intention of a sphere model was to emulate the micro-structures of sintered material by an artificial geometry model. Irregularity can be achieved by embedding stochastic sub-models. The key characteristics of the model of Havemann [28] are:

- A sedimentation approach as introduced by Elsner [32]. Sedimentation is applied along the z-coordinate—the vertical direction in Fig. 5.
- Modularization was implemented by separating the initial spherical layer from the central sedimentation algorithm.
- Irregularity was implemented by stochastic terms in the initialization layer, as well as in the sphere radii.
- Spheres are allowed to overlap randomly in order to achieve smaller porosity values than that of a tight sphere packing.

The initial sphere layer is a hexagonal grid in the xy plane. The position of each sphere in this layer varies statistically. The simulation domain is filled with spheres as long as the center of the spheres are inside the simulation box. The outer spheres in Fig. 5 reach somewhat outside the simulation domain. The key parameters of the sphere model are given in pixels.

1. Domain size (x, y, z) in pixels;
2. Sphere radius min/max;
3. Distance between spheres in the grid of the initial layer;
4. Relative overlay (max), p_overlap in Table 1;
5. Target porosity of the sphere packing.

The 3D model of Havemann [28, 33] generates a tight sphere packing in a rectangular domain according to the parameters above. Often the porosity of the sphere packing is larger than desired for applications regarding to PTLs, as measured by Borah [19]. In such cases the porosity is iterative reduced in a post-processing step of the 3D model. The radii of selected spheres are increased randomly.

Havemann analyzed the irregularity of the resulting sphere packing according to the distribution of the azimuthal and polar angles between neighboring spheres [28]. She found that the overlap factor should be larger than 0.02, relative to the sphere radius, in order to achieve irregular angles between neighbors. The code is available at Jülich DATA, [33] together with more detailed user documentation.

**Table 1** Parameter ranges of the spherical model

| | Radius/µm | Relative distance | p_overlap | Porosity |
|---|---|---|---|---|
| Min | 5 | 0.3 | 0.04 | 0.22 |
| Max | 23 | 0.5 | 0.06 | 0.30 |

### 3.3 Convolutional neural network

As in previous work [24], a CNN can predict the permeability of a micro-structure, which is given by a series of BW images. The foreseen materials for the prediction are PTL structures as introduced in Sect. 2.1 and displayed in Fig. 2. In light of artificial sphere-based geometries and previous investigations by Bukka [34], a domain size of 200 × 200 × 200 was selected for the 3D input layer of the CNN. The domain size is large enough to keep the influence of the wall boundary conditions of the LB simulations low [27]. At a resolution of 1 µm/px the domain size is a multiple of the expected region of interest (ROI). The architecture of the CNN is shown in Fig. 7.

Similar to previous work [24] the major structure of the architecture is a series of 3D convolutional and average pooling layers. The series of convolutional and pooling layers belongs to a fundamental CNN architecture that can identify structures at different scales [35]. Starting with initial 12 channels, the convolutional layers double the number of channels while the pooling layers reduce the size of the 3D structure by a factor of two in each direction. Low-level features can be captured by the top filters. The spatial reduction in subsequent layers enables the identification of larger high-level features. Behind a flattening layer the dimensionality of the data was stepwise reduced by dense layers. Their intention is to reduce overfitting [35]. The architecture is similar to that proposed in previous work [24, 36]. The dimensions were adapted to the particular morphology of the sphere-based micro-structures [34].

**Fig. 7** Architecture of the CNN

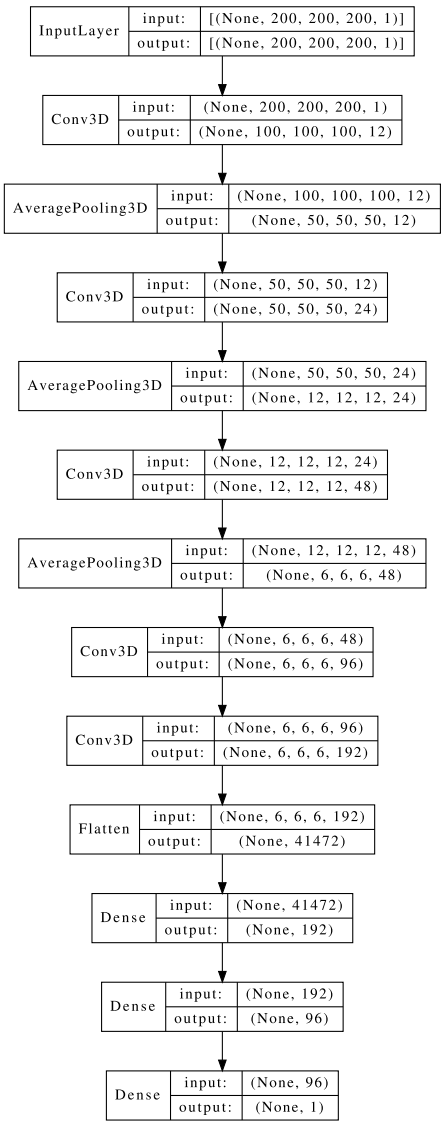

### 3.4 Data preparation

The sphere packings created by the geometric model from Sect. 3.2 are represented as lists as well as a series of BW images. Based on a resolution of 1 µm/px, these image series were taken for the specification of the micro-structure for the LB simulations (Sect. 3.1). The sphere packings were created to fill the given domain in the x and y direction. However, the bottom of the sphere packing is still dominated by the initial layer within the range of two sphere diameters, even in the case of overlapping spheres. This was observed by Havemann when analyzing the distributions of the azimuthal and polar angles between neighboring spheres [28]. Image layers on top are almost empty due to the sedimentation algorithm. For this reason, the simulation domain of the geometric model must be larger in the z-direction than desired for the LB simulation. The desired size for the LB simulation was cut out of the center of the image stack.

Data augmentation was applied by mirroring the 3D data along the x- and y-axes and its rotation around the z-axis. These transformations and their combinations do not affect the calculation of TP characteristics, which increases the amount of available data by a factor of eight. For achieving convergence of the training it was necessary to multiply the permeability $\kappa$ from Eq. (1) by a factor of 100.

### 3.5 Training

The training data consists of 3D image stacks of dimensions $200 \times 200 \times 200$, created by the spherical model (Sect. 3.2). Parameters according to Table 1 were selected in order to achieve porosities in the range of the real material as well as permeabilities that cover the range of real data. The full list of parameters of the sphere model is provided by Havemann and Froning [33], together with an example input file. Because of the stochastic nature of the initial layer of the sphere model, five stochastic realizations of each set of parameters were created. 29 tuples of parameter sets were processed, resulting in 145 micro-structures via the five realizations of each of them. Applying the data augmentation mentioned in Sect. 3.4, the number of data points was increased by a factor of eight, to 1160.

Table 1 shows the range of relevant input parameters of the spherical model. The units of the spherical model were chosen as being 1 µm/px, same as the resolution of the images in Fig. 2. The relative distance and the parameter p_overlap in Table 1 are input parameters of the sphere model [28, 33]. They are related to the maximum radius of the spheres. For each tuple of parameters, the sphere radii varied in a range of 3 µm width. Because the sintering process changes the shape of the particles with potentially larger curvatures than that of the original spheres, the small radii were included in the training data.

## 4 Validation

Five-fold cross-validation was applied to the dataset. All of the data were randomly split into five subsets. As an outcome, there were five alternatives to select one of them as a test set and the others as a training set. In this manner, five folds were randomly defined, each of them consisting of 80% training and 20% test data. The accuracy of the predictions was in the same range for each fold.

During the training, for each fold the hyper parameters were optimized separately, which required a full training run for each set of hyper parameters. The hyper parameters were varied in a grid-based manner according to the following values:

- Batch size: 12, 16, 24;
- Max. learning rate (LR): 0.01, 0.001, 0.0001.

Each combination of the above was applied separately to train the data (of each fold) separately. One optimization run (9 trainings) required 31 min on a node of the HPC system CLAIX at RWTH Aachen University, which is equipped with two GPUs of the Nvidia H100 type. The five folds led to different optimal hyper parameters as shown in Table 2.

The training history is illustrated in Fig. 8. The mean squared error (MSE) is shown separately for the training and validation sets of the five folds. The early stopping criterion of Tensorflow led stop the training at different times for each

**Table 2** Best hyper parameters identified for the folds and resulting losses

| Fold | Batchsize | LR | Losses/$\mu m^4$ | |
|---|---|---|---|---|
| | | | Training | Validation |
| 1 | 16 | 0.0001 | $3.6 \times 10^{-4}$ | $3.9 \times 10^{-4}$ |
| 2 | 16 | 0.0001 | $1.3 \times 10^{-4}$ | $1.8 \times 10^{-4}$ |
| 3 | 12 | 0.001 | $2.9 \times 10^{-4}$ | $1.5 \times 10^{-4}$ |
| 4 | 24 | 0.0001 | $3.9 \times 10^{-4}$ | $4.6 \times 10^{-4}$ |
| 5 | 12 | 0.001 | $1.6 \times 10^{-4}$ | $3.3 \times 10^{-4}$ |

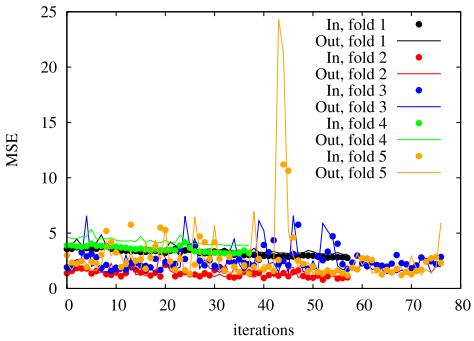


**Fig. 8** Training history

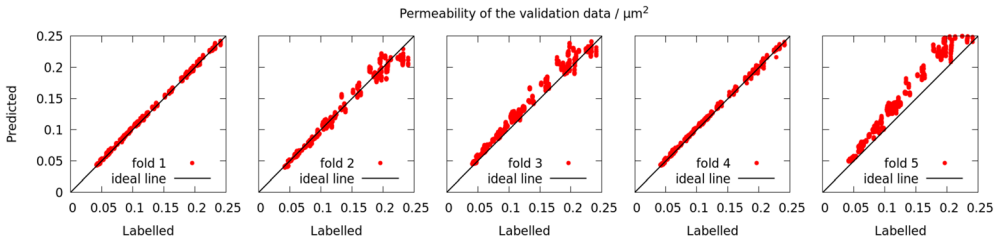


**Fig. 9** Accuracy of the predicted TP permeability of the validation data of folds 1–5

fold. In Fig. 8, folds 3 and 5 look worse than the others. Sometimes during the training the MSE was even larger for the in-sample sets than that of the out-of-sample sets.

Depending on the data, different sets of hyper parameters were identified to create a CNN with the best accuracy for the validation set. The accuracy of the predictions of the validation data of the five folds is shown in Fig. 9.

For each of the five folds the predicted TP permeability was close to the ideal line. In general, small permeability values were predicted more accurately than large ones. However, the folds are of different accuracies. Fold 1 is the most accurate one in this data, whereas the worst seems to be fold 5. The data consists of realizations of the sphere model created with various model parameters. On the other hand, the number of variations in the parameter set is small, only 145 different sets as mentioned in Sect. 3.5. With a random separation of the data into five pieces the ranges of the parameter sets can be distributed inhomogeneously. In such cases the prediction on the validation set may be sub-optimal. Because the separation of the data into five subsets was performed randomly, a new separation would lead to different subsets and therefore to another set of folds. As a result, the particular accuracy is stochastic in nature, and a new attempt may lead to diagrams slightly different from those in Fig. 9. Therefore, it is desirable to have good results in the application of the CNN to real data, not only using the model based on the best fold but also the others.

## 5 Results

From the real data stacks IEK07... IEK92, 50 random subsections of the training size: $200 \times 200 \times 200$ pixels were extracted, and then the TP permeabilities of these were predicted using the ML model. The predictions show a statistical distribution according to the random positions of the subsections. The 0%, 25%, 50%, 75%, and 100% quantiles (quartiles) of the predicted TP permeabilities were then evaluated.

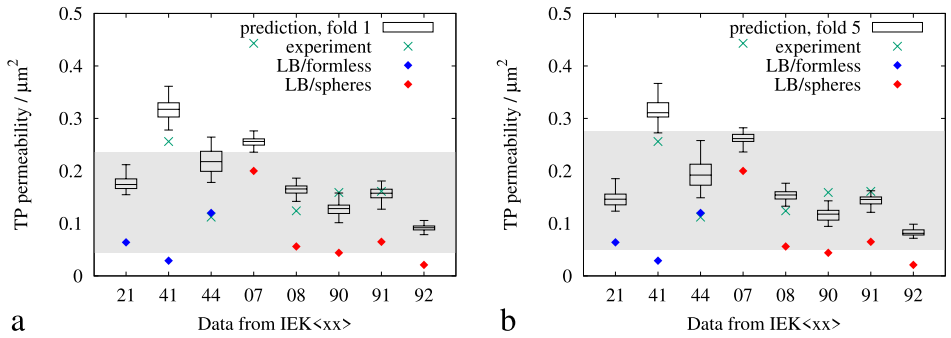


**Fig. 10** Quantiles of predicted permeabilities, applied to real data: **a** fold 1; **b** fold 5. The range of predictions of the training data is shaded gray. Source of the experiments and LB simulation results: Borah [19]

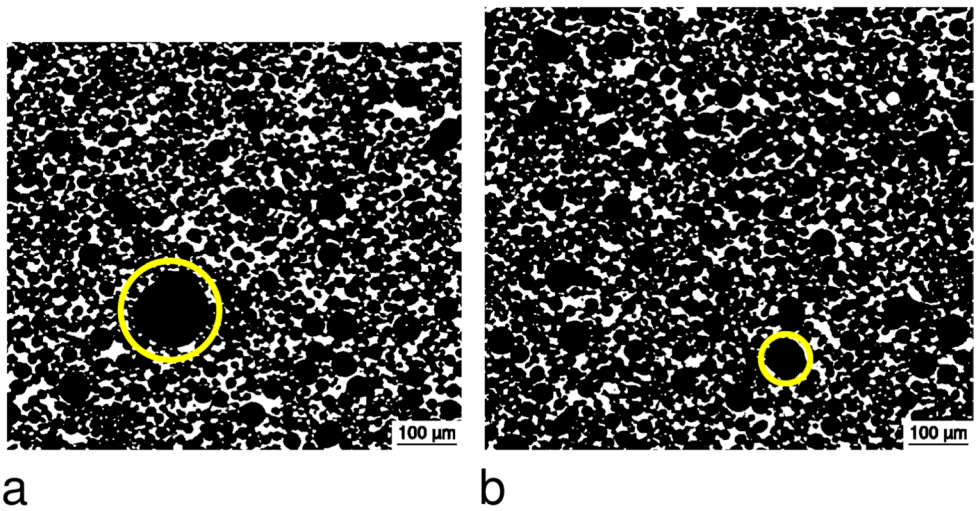


**Fig. 11** Artifacts larger than 45 µm are marked in yellow: **a** IEK08, image 82 of 355; **b** IEK90, image 81 of 350

The predicted TP permeabilities of the subsections encompass the values calculated from LB simulations in the case of IEK07 and IEK41. For IEK41, the predicted permeability values are even beyond the range of the values of the training data. It is notable that the material of IEK21, IEK41, and IEK44 was not built from spherical particles [19]. For folds one and five, the situation is displayed in Fig. 10. These two folds were chosen because fold one looked best in the validation Sect. 4, Fig. 9, and fold five looked the worst. Some of the permeability values are outside the range of the training data, which is shaded gray. Such values indicate that the input images may contain structures that were not covered by the image stacks in the training data. This can be observed in the data of IEK41, IEK44, and IEK07.

The experimental data were taken from Borah [19]. Furthermore, LB simulations were run on all the domains of the micro-structures of IEK07,..., IEK92, as displayed in Fig. 2 and provided by Froning and Müller [29]. The CNN predicted the permeability of 50 subdomains of size 200 µm × 200 µm × 200 µm each. The subdomains were randomly selected from amongst the entire domains of the real micro-structures. According to their positions, the permeabilities show a statistical variation on each of the eight experimental micro-structures, visualized as boxplots in Fig. 10. On IEK07, IEK08, IEK90, IEK91, and IEK92 the variation, displayed as boxplots in Fig. 10, was within a narrower range than those of IEK21, IEK41, and IEK44. This can be explained by the fact that the latter material was created from formless material instead of spherical particles [19]. Furthermore, the predicted permeability values were close to the LB ones in the case of the sphere-based material. For IEK08, IEK90 and IEK91, the predicted permeability is even closer to the experimental data than the LB simulations of the reconstructed micro-structure. For the sphere-based material (IEK07, IEK08, IEK90, IEK91, and IEK92), there is a systematic overestimation of the permeability by the CNN. One reason for such an overestimation might be artifacts in the images of the micro-structures. Based on the fact that the material was sintered from spheres with a diameter of 45 µm [19], the spherical model of Havemann [28] was applied with parameters creating spheres with diameters smaller than or equal to this value. On the other hand, images representing the real data contain sub-structures larger in size. Figure 11 shows two examples where artifacts larger than the original particle size of 45 µm can be observed in the image stacks. Meanwhile, Di Nisio et al. [37] observed an influence of the filling strategy of beads on the resulting permeability and porosity of porous media. Although their beads were not further processed by sintering, such effects

may possibly affect the micro-structure of the material investigated in this manuscript. Whether the filling strategy, as reported by Di Nisio et al., affects the initialization of Havemann's spherical model or, moreover, targets the difference between the sedimentation algorithm and the sintering process, cannot be determined at this stage of the investigation.

The CNN trained with smaller spheres cannot possibly recognize these large sub-structures, but the LB simulations can. In these, the large sub-structures may lead to reduced permeabilities.

From Fig. 9, it can be seen that some permeability values are missing in the training data within the range from 0.15 to 0.2 µm$^2$. However, for the sub-sections of the real data such values were predicted as seen in Fig. 10. This is because the spherical model of Havemann does not represent the entire micro-structure as a whole, but small parts of its artificial structure can be revealed by the hidden layers of the CNN.

The CNN was not successful in predicting the permeability of IEK21, IEK41, and IEK44. Without the background knowledge of how the material was manufactured, the images of all eight samples look similar in Fig. 2. However, the formless material is inherently irregular in its basic structure. Therefore the CNN, which is based on more regular attributes, is less accurate in the prediction of the permeability, as represented by a larger deviation from the true values, as well as a larger statistical variation according to the positions of the sub-domains. Even regular basic structures, e.g., ellipsoids instead of spheres, can change the material properties. Song et al. [38] found a relationship between the shape of elliptical particles and the permeability of porous materials made from them.

Finally, the results, based on five different folds of the underlying data, are not exactly the same. Although Figs. 10a is based on fold one, another set of training data can lead to slightly different results. Figure 12 was processed on a CNN trained separately with folds one to five.

The diagram shows a statistical variation in the prediction that is overlaid to the uncertainties discussed above. It is important that the prediction leads to the same evaluations for each set of training data. Analyzing five folds, a robustness of the CNN in relation to the data can be shown. The boxplots in Fig. 12 are close to each other when the CNN was applied to a particular set of the real PTL data.

The predicted permeability values of the non-sphere-based materials IEK21, IEK41, and IEK44 span a wider range than those of the sphere-based ones.

## 6 Discussion

The TP permeability of the sphere-based PTL material was overestimated by the CNN as shown in Fig. 10. Although the deviation of the ML predictions from the material based on formless particles—IEK21, IEK41 and IEK44—appears random, there is a systematic overestimation for the sphere-based material IEK07, IEK08, IKE90, IEK91, and IEK92. The geometric characteristics of the micro-structure of the sphere-based real material and data used for training are:

The spheres of the training data were dropped down by a sedimentation algorithm, while the particles of the real data were sintered at high temperatures [19]. In the artificial data, the base structures remain spheres, whereas in the real data the base structures can change their shape. Havemann [28] analyzed the angles between neighboring spheres in artificial sphere packing. Although the polar angles were proven to be uniformly distributed, an uniform distribution of the azimuthal angles could be approximated by the model's parameters but not fully achieved. The biggest influence on the accuracy of the CNN predictions is the shape of the base structures. Sphere-based material was predicted more accurately than others. The physical sintering process of the real PTL material is not represented

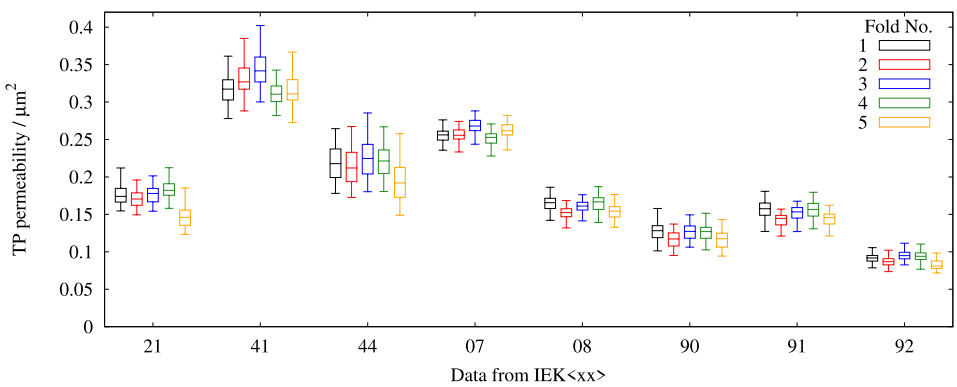


**Fig. 12** Quantiles of predictions of five folds, applied to real data

by the artificial data, which may lead to a systematic deviation between the predicted and true permeabilities. The accuracy of the prediction can possibly be enhanced by distributing the data into training and validation sets in a manner that the parameters of the underlying sphere model are distributed homogeneously across the fold-building subsets. On the other hand it is recommended to split the data into their subsets randomly [35].

The generalization capability of a CNN is the potential to apply it to unseen, new data which has the same distribution as the training set [39]. The results in Fig. 10 show that the generalization is sub-optimal in case the data in IEK<xx>. Overfitting can be one of the possible reasons [39]. According to Fig. 8, overfitting—or another kind of misalignment of the data—might occur on folds 2, 3 and 5. But the deviation of the prediction from LB simulations on the sub-regions of IEK<xx>, shown in Fig. 10, indicate another potential cause of error. For all folds, the permeability predicted by the CNN is larger than that from the LB simulation of the entire domain of IEK<xx>. It can be concluded that there must be a systematic difference between the training and the real data in case of xx$\epsilon\{07, 08, 90, 91, 92\}$. Comparing Figs. 2 and 5, it can be observed that the artificial spheres build sharp edges where they contact each other. Such sharp edges cannot be observed in the real data shown in Fig. 2. That can possibly lead to poor matches in the top layer of the CNN.

## 7 Conclusion

A CNN was trained with micro-structures created by an artificial spherical model. The algorithm represents a sedimentation model that was modified to allow smaller porosities than those of a tight sphere packing. The spherical model generated artificial micro-structures that look somehow similar as BW images taken from real material that was manufactured by sintering titanium particles. The trained CNN was applied to image series representing the real data of the micro-structure of the sintered titanium PTLs of electrolyzers. Although the overlapping algorithm differed from the physical behavior of the sintering process, the CNN was able to predict the permeability with a reasonable degree of accuracy. The prediction of the CNN is less accurate for PTLs that were manufactured from particles of different shapes. The results show that the prediction of the permeability of sintered titanium material by a CNN is possible. That can save a large amount of computing resources compared to LB simulations. For a real-world application it is essential to ensure that the material was manufactured from spherical particles. The sintered material could be represented by stochastic ensembles of an artificial sphere model. Sinter processes are often also used in manufacturing porous material for other applications, e.g., for solid oxide fuel cells and electrolyzers [40].

**Acknowledgements** The transport simulations of the real material, as presented by Borah [19], were formerly run on JURECA [41]. Transport simulations on the sphere model were run on CLAIX within the NHR project p0020317. The training of the ML model was performed using GPU nodes of CLAIX.

The authors gratefully acknowledge the computing time provided to them at the NHR Center NHR4CES at RWTH Aachen University (project number p0020317). This is funded by the Federal Ministry of Education and Research, and the state governments participating on the basis of the resolutions of the GWK for national high performance computing at universities.

The authors thank Christopher Wood for proofreading the manuscript.

**Author contributions** D.F. developed the concept and wrote the main manuscript text. E.H. and M.M. provided the experimental data, E.H. discussed about the validation. R.P. supervised the investigation.

**Funding** This research was funded by the Deutsche Forschungsgemeinschaft (DFG, German Research Foundation)—491111487.

**Data availability** Data is available from Froning and Müller [29].

**Code availability** The code for generating sphere packings is provided by Havemann and Froning [33].

**Materials availability** Not applicable.

### Declarations

**Ethics approval and consent to participate** Not applicable.

**Consent for publication** Not applicable.

**Competing interests** The authors declare no competing interests.

**Open Access** This article is licensed under a Creative Commons Attribution-NonCommercial-NoDerivatives 4.0 International License, which permits any non-commercial use, sharing, distribution and reproduction in any medium or format, as long as you give appropriate credit to the original author(s) and the source, provide a link to the Creative Commons licence, and indicate if you modified the licensed material. You do not have permission under this licence to share adapted material derived from this article or parts of it. The images or other third party material in this article are included in the article's Creative Commons licence, unless indicated otherwise in a credit line to the material. If material is not included in the article's Creative Commons licence and your intended use is not permitted by statutory regulation or exceeds the permitted use, you will need to obtain permission directly from the copyright holder. To view a copy of this licence, visit http://creativecommons.org/licenses/by-nc-nd/4.0/.

## References

1. Gostick JT, Fowler MW, Ioannidis MA, Pritzker MD, Volfkovich YM, Sakars A. Capillary pressure and hydrophilic porosity in gas diffusion layers for polymer electrolyte fuel cells. J Power Sources. 2006;156(2):375–87. https://doi.org/10.1016/j.jpowsour.2005.05.086.
2. Hussaini IS, Wang CY. Measurement of relative permeability of fuel cell diffusion media. J Power Sources. 2010;195(12):3830–40. https://doi.org/10.1016/j.jpowsour.2009.12.105.
3. Pant LM, Mitra SK, Secanell M. Absolute permeability and Knudsen diffusivity measurements in PEMFC gas diffusion layers and micro porous layers. J Power Sources. 2012;206:153–60. https://doi.org/10.1016/j.jpowsour.2012.01.099.
4. Tomadakis MM, Robertson TJ. Viscous permeability of random fiber structures: comparison of electrical and diffusional estimates with experimental and analytical results. J Compos Mater. 2005;39(2):163–88. https://doi.org/10.1177/0021998305046438.
5. Nabovati A, Hinebaugh J, Bazylak A, Amon CH. Effect of porosity heterogeneity on the permeability and tortuosity of gas diffusion layers in polymer electrolyte membrane fuel cells. J Power Sources. 2014;248:83–90. https://doi.org/10.1016/j.jpowsour.2013.09.061.
6. Froning D, Drakselová M, Tocháčková A, Kodým R, Reimer U, Lehnert W, Bouzek K. Anisotropic properties of gas transport in non-woven gas diffusion layers of polymer electrolyte fuel cells. J Power Sources. 2020;452: 227828. https://doi.org/10.1016/j.jpowsour.2020.227828.
7. Zhang S, Hess S, Marschall H, Reimer U, Beale S, Lehnert W. openfuelcell2: a new computational tool for fuel cells, electrolyzers, and other electrochemical devices and processes. Comput Phys Commun. 2024;298: 109092. https://doi.org/10.1016/j.cpc.2024.109092.
8. Teng Y, Li Z, Chen C. A comprehensive review of pre-Darcy flows in low-permeability porous media. arXiv; 2024. https://doi.org/10.48550/ARXIV.2401.04930.
9. Janßen H, Holtwerth S, Zwaygardt W, Stähler A, Behr W, Federmann D, Carmo M, Lehnert W, Müller M. A facile and economical approach to fabricate a single-piece bipolar plate for PEM electrolyzers. Int J Hydrog Energy. 2024;49:816–28. https://doi.org/10.1016/j.ijhydene.2023.09.175.
10. Beale SB, Andersson M, Weber N, Marschall H, Lehnert W. Combined two-phase co-flow and counter-flow in a gas channel/porous transport layer assembly. ECS Trans. 2020;98(9):305–15. https://doi.org/10.1149/09809.0305ecst.
11. Yuan X-Z, Shaigan N, Song C, Aujla M, Neburchilov V, Kwan JTH, Wilkinson DP, Bazylak A, Fatih K. The porous transport layer in proton exchange membrane water electrolysis: perspectives on a complex component. Sustain Energy Fuels. 2022;6(8):1824–53. https://doi.org/10.1039/d2se00260d.
12. Panchenko O, Borgardt E, Zwaygardt W, Hackemüller FJ, Bram M, Kardjilov N, Arlt T, Manke I, Müller M, Stolten D, Lehnert W. In-situ two-phase flow investigation of different porous transport layer for a polymer electrolyte membrane (PEM) electrolyzer with neutron spectroscopy. J Power Sources. 2018;390:108–15. https://doi.org/10.1016/j.jpowsour.2018.04.044.
13. Parra-Restrepo J, Bligny R, Dillet J, Didierjean S, Stemmelen D, Moyne C, Degiovanni A, Maranzana G. Influence of the porous transport layer properties on the mass and charge transfer in a segmented PEM electrolyzer. Int J Hydrog Energy. 2020;45(15):8094–106. https://doi.org/10.1016/j.ijhydene.2020.01.100.
14. Park S, Lee W, Na Y. Performance comparison of proton exchange membrane water electrolysis cell using channel and PTL flow fields through three-dimensional two-phase flow simulation. Membranes. 2022;12(12):1260. https://doi.org/10.3390/membranes12121260.
15. Lopata JS, Weidner JW, Cho H-S, Tippayawong N, Shimpalee S. Adjusting porous media properties to enhance the gas-phase OER for PEM water electrolysis in 3D simulations. Electrochim Acta. 2022;424: 140625. https://doi.org/10.1016/j.electacta.2022.140625.
16. Schuler T, De Bruycker R, Schmidt TJ, Büchi FN. Polymer electrolyte water electrolysis: correlating porous transport layer structural properties and performance: Part I. Tomographic analysis of morphology and topology. J Electrochem Soc. 2019;166(4):270–81. https://doi.org/10.1149/2.0561904jes.
17. Chen Y-C, Karageorgiou C, Eller J, Schmidt TJ, Büchi FN. Determination of the porosity and its heterogeneity of fuel cell microporous layers by x-ray tomographic microscopy. J Power Sources. 2022;539: 231612. https://doi.org/10.1016/j.jpowsour.2022.231612.
18. Höh M. Poröse Transportschichten für die Polymerelektrolytmembran-Wasserelektrolyse. PhD thesis, RWTH Aachen; 2017. https://juser.fz-juelich.de/record/838672
19. Borah D. Two-phase flow in porous transport layers of polymer electrolyte membrane electrolysers. PhD thesis, RWTH Aachen; 2021. https://juser.fz-juelich.de/record/894583
20. Xu C, Wang J, Wang J, Yang K, Li G, Gao W, Wang H, Zhao S. Structural optimization study on porous transport layers of sintered titanium for polymer electrolyte membrane electrolyzers. Appl Energ. 2024;357: 122541. https://doi.org/10.1016/j.apenergy.2023.122541.
21. Bhaskaran S, Pandey D, Surasani VK, Tsotsas E, Vidakovic-Koch T, Vorhauer-Huget N. LBM studies at pore scale for graded anodic porous transport layer (PTL) of PEM water electrolyzer. Int J Hydrog Energy. 2022;47(74):31551–65. https://doi.org/10.1016/j.ijhydene.2022.07.079.
22. Liu J, Kerner F, Schlüter N, Schröder D. Predicting the topological and transport properties in porous transport layers for water electrolyzers. ACS Appl Mater Interfaces. 2023;15(46):54129–42. https://doi.org/10.1021/acsami.3c12345.
23. Cawte T, Bazylak A. A 3d convolutional neural network accurately predicts the permeability of gas diffusion layer materials directly from image data. Curr Opin Electrochem. 2022;35: 101101. https://doi.org/10.1016/j.coelec.2022.101101.

24. Froning D, Hoppe E, Peters R. The applicability of machine learning methods to the characterization of fibrous gas diffusion layers. Appl Sci. 2023;13(12):6981. https://doi.org/10.3390/app13126981.
25. Kamrava S, Tahmasebi P, Sahimi M. Linking morphology of porous media to their macroscopic permeability by deep learning. Transp Porous Med. 2019;131(2):427–48. https://doi.org/10.1007/s11242-019-01352-5.
26. Qian M, Zhou J, Wang J, Ruan L, Xiang Z, Hu X. Permeability prediction of complex porous materials by conjugating generative adversarial and convolutional neural networks. Comput Mater Sci. 2024;238: 112942. https://doi.org/10.1016/j.commatsci.2024.112942.
27. Froning D, Brinkmann J, Reimer U, Schmidt V, Lehnert W, Stolten D. 3D analysis, modeling and simulation of transport processes in compressed fibrous microstructures, using the lattice boltzmann method. Electrochim Acta. 2013;110:325–34. https://doi.org/10.1016/j.electacta.2013.04.071.
28. Havemann K. Erzeugen von Kugelpackungen mit vorgegebener Größenverteilung zur Darstellung von porösen Sinterkörpern in der Simulation von Elektrolyseuren. Bachelor's thesis, University of Applied Sciences, Aachen, Germany; 2022. https://doi.org/10.34734/FZJ-2023-01025
29. Froning D, Müller M. Micro-structure of porous transport layers of polymer electrolyte membrane electrolysers. Jülich DATA; 2024. https://doi.org/10.26165/JUELICH-DATA/PPAL4B
30. Hackemüller FJ, Borgardt E, Panchenko O, Müller M, Bram M. Manufacturing of large-scale titanium-based porous transport layers for polymer electrolyte membrane electrolysis by tape casting. Adv Eng Mater. 2019. https://doi.org/10.1002/adem.201801201.
31. Panchenko U, Arlt T, Manke I, Müller M, Stolten D, Lehnert W. Synchrotron radiography for a proton exchange membrane (pem) electrolyzer. Fuel Cells. 2020;20(3):300–6. https://doi.org/10.1002/fuce.201900055.
32. Elsner A. Computergestützte Simulation und Analyse zufälliger dichter Kugelpackungen. PhD thesis, Technische Universität Bergakademie Freiberg, Germany; 2009.
33. Havemann K, Froning D. Erzeugen von Kugelpackungen mit vorgegebener Größenverteilung zur Darstellung von porösen Sinterkörpern in der Simulation von Elektrolyseuren. Jülich DATA; 2024. https://doi.org/10.26165/JUELICH-DATA/ZTVRNO
34. Bukka V. Machine learning for the characterization of the micro-structure of the porous transport layers of electrolyzers. Master's thesis, Universität Siegen, Germany; 2023.
35. Géron A. Hands-on machine learning with scikit-learn, keras, and TensorFlow. Second edition edn. Beijing: O'Reilly; 2019.
36. Froning D, Wirtz J, Hoppe E, Lehnert W. Flow characteristics of fibrous gas diffusion layers using machine learning methods. Appl Sci. 2022;12(23):12193. https://doi.org/10.3390/app122312193.
37. Di Nisio FG, Alves TA, Volpato N. Permeability and porosity analysis of a unique porous media obtained by bead width variation in a mex filling strategy. Transp Porous Med. 2024;151(7):1627–41. https://doi.org/10.1007/s11242-024-02087-8.
38. Song H, Xie J, Yin P, Fu H, Zhang Y, Yan C. The investigation of the particle shape effect on the permeability of porous media through lattice Boltzmann simulation and experimental study. Int J Therm Sci. 2024;201: 108983. https://doi.org/10.1016/j.ijthermalsci.2024.108983.
39. Urolagin S, Prema KV, Reddy NVS. Generalization capability of artificial neural network incorporated with pruning method. London: Springer; 2012. p. 171–8. https://doi.org/10.1007/978-3-642-29280-4_19.
40. Li W, Wu S, Zhu J, Zhang W, Guan W, Li J. Real-time deformation and stress response of the planar SOFC during sintering. J Eur Ceram Soc. 2024;44(4):2242–50. https://doi.org/10.1016/j.jeurceramsoc.2023.11.057.
41. Krause D, Thörnig P. JURECA: modular supercomputer at Jülich supercomputing centre. J Large Scale Rese Facilities. 2018;4:132. https://doi.org/10.17815/jlsrf-4-121-1.

**Publisher's Note** Springer Nature remains neutral with regard to jurisdictional claims in published maps and institutional affiliations.